shell. For example, the morphology of structures observed in the western component of the optical outflow from Cepheus A (the GGD37 complex[27]) is similar to the structures observed in Fig. 1. The fragmentation of HH2 into distinct clumps[28] could also have been caused by processes similar to those studied here. In many cases (such as HH2) the acceleration of the shell that leads to fragmentation into clumps might not necessarily be caused by variability of the source, but might be caused by very steep (that is, $n>2$) density gradients associated with the edges of molecular clouds.

The hydrodynamical processes that lead to fragmentation into bullets in OMC-1 are not confined merely to outflows from young stars. For example, there is a wide variety of hydrodynamical instabilities in the evolution of a supernova shell that can lead to fragmentation and the formation of bullets in these systems as well. The shell of ambient material swept up by the blast wave is subject to a radiative overstability[22], the thin-shell instability[24], and to the R–T instability in the early phases of its evolution[29]. Moreover, at the centre of the remnant, the ejecta arising from the stellar envelope is R–T-unstable during the acceleration phase[30] and is subject to convective instabilities[31], which both mix the ejecta and cause it to become clumpy. Finally, if a pulsar is formed in the supernova event, the expansion of a synchrotron nebula created by the spin-down of the pulsar can lead to acceleration of the ejecta during the early phase of evolution of the remnant. Such acceleration is yet another mechanism for producing fragmentation. In fact, the dense and long fingers of ejecta observed inside the Crab supernova remnant by the Hubble Space Telescope (HST) are best interpreted as being caused by a magnetic R–T instability as the ejecta is accelerated by the magnetized synchrotron nebula inflated by the Crab pulsar[3]. The velocity of the knots associated with the fingers in the Crab filaments is about 2,000 km s^{-1}. Using the Sedov-Taylor similarity solution[16] to describe the growth of the blast wave, and assuming an ambient density of $N_H = 1$ cm^{-3}, we find that the knots will strike the blast wave in 3,000 years assuming that they maintain their current velocity. Remarkably, recent X-ray observations of the Vela supernova remnant[2] have revealed a structure identified as a bullet that has punctured the blast wave and is now propagating into the ambient ISM. The observed velocity of the bullet and the age of the Vela remnant are in good agreement with the time calculated above for knots of ejecta to impact the blast wave. Thus we propose that processes similar to those observed in the Crab are responsible for forming the bullet discovered in Vela.

Over long timescales, variations in the mass loss rate in winds associated with massive stars can produce structures in the circumstellar gas that resemble bullets. Detailed two-dimensional hydrodynamical calculations[25] of a time-variable wind produced by evolution of the central star from the main sequence through the luminous blue variable stage and into the onset of the Wolf–Rayet stage are strikingly similar to the results presented here for protostellar winds.

New observations of planetary nebula indicate that these outflows may also form dense knots. For example, recent HST observations of NGC6543 reveal a complex system of knots and filaments in this source[32]. The observed line ratios indicate that the density, temperature and ionization balance are highly variable in the outflow, and it is likely that hydrodynamical processes have led to the clumpy nature of the nebula. Therefore, although supersonic bullets are associated with a very wide variety of astrophysical outflow sources, it would appear that similar hydrodynamical processes are responsible for their formation in each case. □

Received 27 April; accepted 21 August 1995.

1. Allen, D. A. & Burton, M. G. *Nature*, **363,** 54–56 (1993).
2. Strom, R., Johnston, H. M., Verbundt, F. & Aschenback, B. *Nature* **373,** 590–592 (1995).
3. Hester, J. J. *et al. Astrophys. J.* (in the press).
4. Bachiller, R. & Gomez-Gonzales, J. *Astr. Astrophys. Rev.* **3,** 257–287 (1992).
5. Edwards, S., Ray, T. & Mundt, R. in *Protostars and Planets III* (ed. Levy, E. & Lunine, J.) 567–602 (Univ. Arizona Press, Tuscon, 1994).
6. Norman, C. & Silk, J. *Astrophys. J.* **228,** 197–205 (1979).
7. Stone, J. M. & Norman, M. L. *Astrophys. J.* **420,** 237–246 (1994).
8. de Gouveai Dal Pino, E. & Benz, W. *Astrophys. J.* **410,** 686–695 (1993).
9. Riepurth, B. *Nature* **340,** 42–45 (1989).
10. Stone, J. M. & Norman, M. L. *Astrophys, J.* **413,** 210–220 (1993).
11. Raga, A. C. *Rev. Mex. Astr. Astrofys. serie de conferencias* **1,** 103–117 (1995).
12. Scoville, N., Kleinmann, S. G., Hall, D. N. B. & Ridgway, S. T. *Astrophys. J.* **275,** 201–224 (1983).
13. Genzel, R. & Stutzki, J. *A. Rev. Astr. Astrophys.* **27,** 41–85 (1989).
14. Bunn, J. C., Hoare, M. G. & Drew, J. E. *Mon. Not. R. astr. Soc.* **272,** 346–354 (1995).
15. Martì, J., Rodriguez, L. F. & Riepurth, B. *Astrophys. J.* **449,** 184–187 (1995).
16. Spitzer, L. Jr. *Physical Processes in the Interstellar Medium* (Wiley-Interscience, New York, 1978).
17. Castor, J., McCray, R. & Weaver, R. *Astrophys. J.* **200,** L107–L110 (1975).
18. Weaver, R., McCray, R., Castor, J., Shapiro, P. & Moore, R. *Astrophys. J.* **218,** 377–395 (1977).
19. Koo, B. C. & McKee, C. *Astrophys. J.* **388,** 93–102 (1992).
20. MacLow, M.-M., McCray, R. & Norman, M. *Astrophys. J.* **337,** 141–154 (1989).
21. Tomisaka, K. & Ikeuchi, S. *Astrophys. J.* **330,** 695–717 (1988).
22. Gaetz, T., Edgar, R. J. & Chevalier, R. A. *Astrophys. J.* **329,** 927–942 (1988).
23. Howarth, I. & Prinja, R. K. *Astrophys. J. Suppl.* **69,** 527–592 (1989).
24. MacLow, M.-M. & Norman, M. L. *Astrophys. J.* **407,** 207–218 (1993).
25. Garciia-Segura, G., MacLow, M.-M. & Langer, N. *Astr. Astrophys.* (in the press).
26. Tedds, J. A., Brand, P. W. J. L., Burton, M. G., Chrysostomou, A. & Fernandes, A. J. L. in *Cloud Cores and Low Mass Stars* (Clemens, D. P. & Barvainis, R.) 375–379 (Astr. Soc. Pacific Conf. Series, 65, San Francisco, 1995).
27. Staude, H. J. & Elsasser, H. *Astr. Astrophys. Rev.* **5,** 165–238 (1993).
28. Schwartz, R. D. *et al. Astr. J.* **106,** 740–746 (1993).
29. Gull, S. F. *Mon. Not. R. astr. Soc.* **161,** 47–69 (1973).
30. Chevalier, R. A. & Klein, R. *Astrophys. J.* **219,** 994–1007 (1977).
31. Herant, M. & Benz, W. *Astrophys. J.* **370,** L81–L84 (1991).
32. Harrington, P. *Bull. Am. astr. Soc.* **26,** 1469 (1995).

ACKNOWLEDGEMENTS. We thank P. Brand and J. Tedds for discussions of observations of OMC-1, and M.-M. MacLow and T. Ray for suggesting improvements to the manuscript.

White-light velocimetry

David J. Erskine & Neil C. Holmes

Lawrence Livermore National Laboratory, 5000 East Avenue, Livermore, California 94551, USA

RADIATION reflected from a moving object experiences a Doppler shift in its frequency. This basic phenomenon underlies practical interferometric techniques for remote velocity measurement used widely in meteorology and law enforcement, as well as in medicine[1] (using acoustic waves) and other fields of science and engineering[2–5]. Existing velocimetric techniques use coherent quasi-monochromatic sources of illumination, which, for optical applications, generally limits practical sources to lasers operating in single-frequency mode. Such sources are not, however, sufficiently powerful for applications where simultaneous velocity measurements at many points on a target are desired. Here we describe a technique for remote velocity measurement that uses broadband incoherent illumination. The viability of this technique is demonstrated by measuring the velocity of a target moving at 16 m s^{-1} using white light from an incandescent source. Powerful, compact and inexpensive radiation sources (such as flash and arc lamps, or lasers operating at several wavelengths) can now be exploited for high-power applications of remote-target velocimetry.

The VISAR[2–5] velocimeter (velocity interferometer system for any reflector) is an optical interferometer having a fixed delay τ between its arms. This delay converts small Doppler shifts into fringe shifts in the interferometer output. Let the delay be specified by the distance ($c\tau$) that light travels in that time, where c is the velocity of light in vacuum. The idealized velocity per fringe proportionality[2,3] (η) of a VISAR is

$$\eta = c\lambda/2c\tau \qquad (1)$$

where λ is the average wavelength of light. For example, to measure highway velocities in green light with $\eta = 10$ m s^{-1} requires $c\tau \approx 8$ m. Equation (1) neglects dispersion[3] in the glass optics inside the interferometer and assumes that $v/c \ll 1$.

In previous VISARs, the coherence length (Λ) of the illumination must be as large as $c\tau$ to produce fringes with significant

visibility. This severely restricted the kind of light source that could be used. The Λ of white light ($\sim$1.5 μm) was insufficient. Previously, lasers have been the only light sources used in VISARs because their coherence length could be made sufficiently long when operated in a single-frequency mode. However, in this mode the output power is low.

Because of this, typical laboratory measurements in shock physics were limited to measurement of velocity at a single point on the target. These experiments[6-8] can measure both the structure and arrival time of a shock wave after propagating through a sample—information that can yield the equation of state (pressure against volume), the transition between elastic and plastic flow (controlled by material strength), or the presence of phase transitions[6,7].

Such experiments could be greatly improved if we could measure sample velocity simultaneously at more than one point. For example, multipoint velocimetry on a wedged sample could show the evolution of the shockwave profile against propagation depth. Moreover, measurements of velocity across a line or an area over a target could diagnose the chaotic motion of an accelerated and spatially perturbed interface between materials of unequal densities (called Rayleigh–Taylor[9] or Richtmeyer–Meshkov[10] instability, depending on the details of the acceleration). This issue is relevant to implosions used in laser fusion.

Previously, multipoint or line[11] VISAR velocimetry has been very expensive. Lasers with sufficiently long coherence length were relatively weak, and required optical amplifiers to illuminate more than a single point. Velocimetry over a surface, or of a remote object through a telescope in the field, demands orders of magnitude more power, particularly if scale coherence lengths of many metres are needed (such as needed for resolving $\sim$10 m s^{-1} velocities).

We have developed a simple and generic method (Fig. 1) of preparing any wave source, regardless of its initial coherence, to illuminate a velocity interferometric experiment. A coherent echo is imprinted on the illuminating light by an interferometer (denoted the source interferometer) having a delay τ_s. The reflected light from the target is observed through a second interferometer (denoted the detecting interferometer) having delay

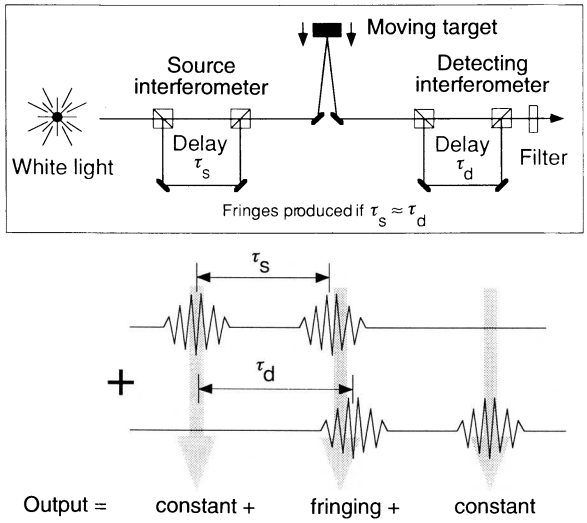

FIG. 1 White-light velocimeter concept. Two interferometers before and after the target have similar delays τ_s and τ_d. White light is a series of independent wave packets. The first interferometer splits each wave packet into two identical packets; the second does the same to create a total of four. Two of these packets will overlap if $\tau_s \approx \tau_d$, producing fringes. The other packets contribute constant intensity. The target's velocity will change the apparent τ_s owing to the Doppler effect, causing a fringe shift. The wave-packet length is inversely proportional to system bandwidth, represented by the filter.

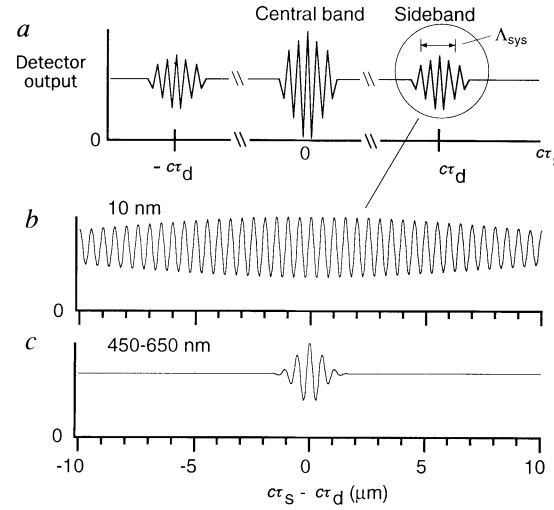

FIG. 2 White-light velocimeter output plotted against source-interferometer delay length ($c\tau_s$), for a stationary target. Both source and detecting interferometers are of the Michelson type. A moving target Doppler-shifts the apparent $c\tau_s$ by $\Delta(c\tau_s) = -(2v/c)(c\tau_s)$. *a*, Diagram of global behaviour: sidebands have the same shape and width as the central band, but lower amplitude. Their width, the system coherence length (Λ_{sys}), is inversely proportional to the bandwidth of the system spectra. *b*, Calculated detail for 495–505-nm gaussian system spectra. *c*, As *b*, but for 450–650 nm bandwidth.

τ_d. Partial fringes result when $c\tau_s$ and $c\tau_d$ are within a coherence length of each other. Target velocity causes the apparent value of τ_s to change owing to the slight Doppler scaling of the spectrum reflected from the target, producing a fringe shift.

Double-interferometer arrangements using short-coherence-length light have been used previously in communication[12] and to multiplex serial fibre optic sensors[13], and to measure target motion where the target is internal to one of the interferometers[14-16]. But we believe we are the first to apply this concept to moving targets external to an interferometer. This allows the fringe phase to be independent of target distance, surface roughness, and the scattering and dispersive properties of the interposed medium. A single-interferometer technique by Geindre *et al.*[17] measures high-velocity (100 km s^{-1}) plasma by illuminating the plasma with two subpicosecond pulses separated by $\sim$1 ps, then dispersing the reflected light with a grating. Their Doppler shift is resolvable by a grating rather than a second interferometer because it is so large.

In general, there is no restriction on the design of either interferometer. However, interpretation of the fringe shift is most straightforward when the detecting interferometer is of a Michelson type. In our demonstration, the same optical system performs the functions of both the source and the detecting interferometers. This makes alignment much easier, because $\tau_s \approx \tau_d$ automatically. However, in applications where the illumination is very much brighter than the light reflected from the target, the source and detecting interferometers should be separate to isolate the glare of illuminating light from shared optics.

The Doppler effect scales the spectrum of the source interferometer by a factor $(1+2v/c)$. Because this spectrum's periodicity is controlled by τ_s, this is equivalent to scaling the apparent value of τ_s to $\tau_s/(1+2v/c)$. Hence, there is an apparent shift in $c\tau_s$ of

$$\Delta(c\tau_s) = \frac{c\tau_s}{1+2v/c} - c\tau_s \cong -\left(\frac{2v}{c}\right)c\tau_s \qquad (2)$$

Figure 2 shows the calculated fringes plotted against $c\tau_s$, for Michelson source and detecting interferometers and a stationary

target. Fringe behaviour with velocity is obtained from these curves by shifting the initial value of $c\tau_s$ by the amount $\Delta(c\tau_s)$ given by equation (2).

The fringe visibility is defined as $(I_{max}-I_{min})/(I_{max}+I_{min})$, where I_{max} and I_{min} are local maximum and minimum output intensities. As Fig. 2 shows, to obtain significant fringe visibility one needs $c\tau_s \approx c\tau_d$, within a distance we call the system coherence length Λ_{sys}, where $\Delta\lambda$ is the bandwidth of the entire system including the detector. For Michelson source and detecting interferometers, the fringe visibility does not exceed 50%. This is not a practical difficulty: because the two outputs of the detecting interferometer are of opposite phase, if they are both recorded they can be subtracted numerically to cancel the non-fringing signal portion. Also, using a Fabry–Perot source interferometer can increase fringe visibility arbitrarily at the expense of decreased absolute signal amplitude, depending on the Fabry–Perot mirror reflectivity R.

We demonstrate white-light velocity interferometry by photographing the fringes from a 16 m s^{-1} moving target with incandescent light. Velocities of this order are more challenging to measure than velocities of order 1 km s^{-1} because of the smaller Doppler shifts. These are resolved by larger values of $c\tau$, which in turn require larger-diameter optics for a given angular field of view. Figure 3 describes our white-light velocimeter having $c\tau_s \approx c\tau_d = 4$ m and $\eta \approx 19$ m s^{-1} per fringe. By retro-reflecting the light from the target the functions of the source and detecting Michelson interferometers are accomplished by the same optics. This automatically ensures that $\tau_d \approx \tau_s$. The interferometer mirrors are misaligned slightly to produce a ladder of fringes to make them more apparent.

An interferometer delay of 4 m is accomplished by the optics enclosed by the dashed box in Fig. 3. These create a virtual plane mirror, from a ray-tracing aspect, but a delay of 4 m in the time of flight of a wave packet. The target was an electric fan with reflective tape on its blades. The beam intercepted the blade from 45 to 54 mm radius, at an angle to the rotation plane of 20.5°. The frequency of rotation was determined stroboscopically to be 53.8 Hz. This yields a velocity component of 15.7 ± 0.3 m s^{-1} parallel to the light. (The uncertainty is in the average fan radius struck by the beam.)

Figure 4 compares photographs of fringes from the stationary and the moving target. The fringe pattern has visibly shifted

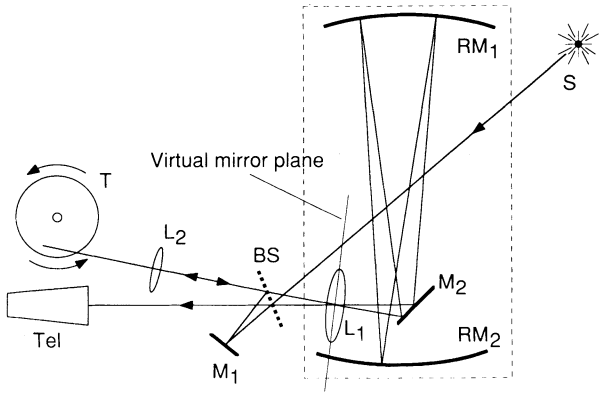

FIG. 3 White-light velocimeter with 4-m delay and $\eta \approx 10$ m s^{-1} per fringe. S, incandescent lamp; T, target is fan with reflective tape on blades; Tel, telescope or camera; BS, 50% beamsplitter; M_1, M_2, plane mirrors; RM_1, RM_2, mirrors with a 1-m radius of curvature separated by 1 m; L_1, 1-m focal-length lens. The optical system in the dashed box acts as virtual plane mirror at a position superimposed on the reflective image of M_1 about BS. L_2, lens imaging the target to the virtual mirror plane. Because light retro-reflects from the target, the same optics perform the functions of the source and the detecting interferometers. The other interferometer output (not used here) travels toward the source and is accessible by inserting a beamsplitter between BS and S.

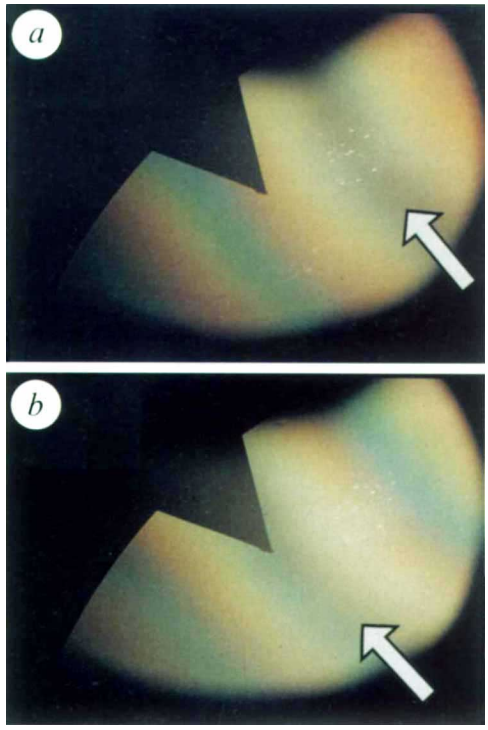

FIG. 4 White-light fringes of the target. *a*, Stationary target; *b*, target moving at 15.7 m s^{-1}. Triangle silhouette at image plane (RM_1) provides a reference location. The dark central fringe (white arrows) can be distinguished by its colourless grey appearance and symmetrical placement relative to the coloured fringes, particularly the red fringes. From *a* to *b* the central fringe has shifted toward the triangle. When viewed in 500-nm light the shift is 0.85 fringe. The bright flecks are dust specks on RM_1 illuminated by the source beam.

toward the reference triangle owing to target velocity. Observation through a 40-nm-wide 500-nm bandpass filter shows the fringe shift to be 0.85 ± 0.07. For $c\tau = 4$ m and $\lambda = 500$ nm, $\eta = 18.7$ m s^{-1} per fringe from equation (1). This yields an interferometrically measured velocity of 15.9 ± 1 m s^{-1}. This agrees with the 15.7 ± 0.3 m s^{-1} measured stroboscopically.

The significance of this demonstration is twofold. First, we observe fringes from an incoherent source with an interferometer delay greatly exceeding the ~1.5 μm coherence length of white light. Second, we demonstrate a fringe shift with target velocity, and this is a low velocity (by shock physics standards) measured remotely with easily obtained optics and an inexpensive light source.

Because a conventional VISAR uses monochromatic illumination, a discontinuous velocity jump will cause an ambiguity in the fringe shift by an integer. This because fringes are periodic. But in the white-light velocimeter, by recording fringe shifts for different colours separately, the velocity can be uniquely determined. One implementation of this is to disperse the velocimeter output by a grating and record the spectrum versus time by a multichannel detector or streak camera. The number of fringes across the streak record in the wavelength direction scales with the velocity, and therefore the velocity skip across the shock is determinate.

Our demonstration measured the velocity of a small area of the fan blade because of the limited angular field of view afforded by the optics we had on hand. We are constructing a new velocimeter with separate source and detecting interferometers, which will allow much brighter illumination with a wider field of view.

The white-light velocimeter should lead to many new applications of velocimetry made practical by inexpensive or powerful incoherent sources. For example, a fluid's velocity field could be measured over a large area on a microsecond or nanosecond

timescale to high precision. This could aid in the study of turbulence. The ultimate spatial resolution would be superior to conventional fluid Doppler velocimetry[18] (where particles cross a standing fringe pattern formed by intersecting laser beams) because the speckle of white light is negligibly small, and because this fluid technique is limited to measurement at a single point. Interferometers implemented with single-mode optical fibre having kilometre delays could measure velocities of order 1 mm s^{-1}, although for a single target point. Such velocity sensitivity has already been demonstrated in a fibre-optic Sagnac[16] interferometer design with a 200-m delay. In our design, the target is external to the interferometer, which allows practical velocimetry of remote targets out of doors. The principle can be applied to other wave phenomena such as microwaves and ultrasound. □

Received 22 May; accepted 14 August 1995.

1. Atkinson, P. & Woodcock, J. P. *Doppler Ultrasound and its Use in Clinical Measurement* (Academic, New York, 1982).
2. Barker, L. M. & Hollenbach, R. E. *J. appl. Phys.* **43,** 4669–4675 (1972).
3. Barker, L. M. & Schuler, K. W. *J. appl. Phys.* **45,** 3692–3696 (1974).
4. Hemsing, W. F. *Rev. scient. Instrum.* **50,** 73–78 (1979).
5. Sweatt, W. *Rev. srient. Instrum.* **63,** 2945–2949 (1992).
6. Erskine, D. J. & Nellis, W. J. *Nature* **349,** 317–319 (1991).
7. Erskine, D. J. & Nellis, W. J. *J. appl. Phys.* **71,** 4882–4886 (1992).
8. Erskine, D. J. & Nellis, W. J. *J. geophys. Res.* **99,** 15529–15537 (1994).
9. Taylor, G. I. *Proc. R. Soc.* A**201,** 192–196 (1950).
10. Richtmeyer, R. D. *Commun. pure appl. Math.* **13,** 297–319 (1960).
11. Hemsing, W. F. in *Shock Compression of Condensed Matter—1991* (eds Schmidt, S. C. *et al.*) 767–770 (North-Holland, Amsterdam, 1992).
12. Delisle, C. & Cielo, P. *Can. J. Phys.* **53,** 1047–1053 (1975).
13. Brooks, J., Wentworth, H., Youngquist, M., Kim, B. Y. & Shaw, H. *J. Lightwave Tech.* **LT-3,** 1062–1071 (1985).
14. Gusmeroli, V. & Martinelli, M. *Optics Lett.* **16,** 1358–1359 (1991).
15. Ribeiro, A., Santos, J. & Jackson, D. *Rev. scient. Instrum.* **63,** 3586–3589 (1992).
16. Harvey, D., McBride, R., Barton, J. & Jones, J. *Meas. Sci. Technol.* **3,** 1077–1083 (1992).
17. Geindre, J. *et al. Optics Lett.* **19,** 1997–1999 (1994).
18. Lagranja, J. L., Garcí-Palacín, J. I. & Aïsa, L. A. *Opt. Engng* **33,** 2449–2460 (1994).

ACKNOWLEDGEMENTS. This work was performed under the auspices of the US Department of Energy.

Fabrication of hollow porous shells of calcium carbonate from self-organizing media

Dominic Walsh & Stephen Mann*

School of Chemistry, University of Bath, Bath BA2 7AY, UK

A RICH variety of elaborate microscopic skeletal structures composed of inorganic materials are produced in nature[1]. Such complex, three-dimensional structures, if produced synthetically, could find important applications as light-weight ceramics, catalyst supports, biomedical implants and robust membranes for high-temperature separation technology. Here we describe a method for synthesizing hollow porous shells of crystalline calcium carbonate (aragonite) that resemble the coccospheres of certain marine algae. We show that thin cellular frameworks of either mesoporous or macroporous aragonite can be formed from oil–water–surfactant microemulsions supersaturated with calcium bicarbonate, with the pore size determined by the relative concentrations of water and oil. Using micrometre-sized polystyrene beads as the substrate for the microemulsion, hollow spherical shells of the honeycomb architecture can be produced. We propose that these cellular frameworks originate from rapid mineralization of aragonite, with a self-organized foam of oil droplets acting as a structural template, and suggest that similar processes could be of general importance in materials chemistry.

* To whom correspondence should be addressed.

We are interested in discovering chemical routes to the fabrication of inorganic materials with organized hierarchical structure and form, analogous to the exquisite biomineralized architectures fashioned by many single-celled organisms such as coccoliths and radiolarians. In this regard, the use of oil–water–surfactant mixed-phase systems as organized reaction media seems to be a promising approach. The phase behaviour and composition of these systems can be varied extensively, indicating that markedly different inorganic structures and architectures could be fabricated. For example, whereas water-rich hexagonal and cubic phases can direct the formation of mesoporous silicas[2], limited amounts of water in bicontinuous microemulsions can give rise to reticulated frameworks of amorphous silica[3] or calcium phosphate[4]. In the latter case, the macroporous architecture consists of interlinked micrometre-sized crystals, indicating that the length scales of the original microemulsion network and inorganic 'replica' are incommensurate. This sug-

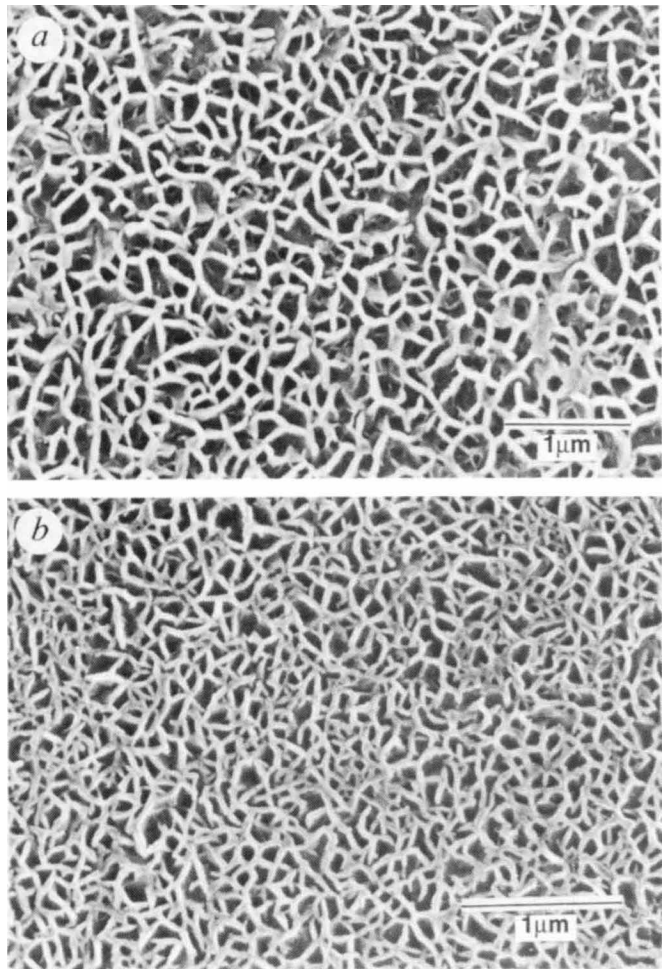

FIG. 1 Scanning electron micrographs of cellular frameworks of aragonite formed on metal substrates. *a*, Product from a bicontinuous microemulsion with a water:oil ratio of 1.4:1, using a tetradecane/hexadecane oil. The average pore size is 225 nm. *b*, Product from tetradecane-containing microemulsion with a water:oil ratio of 0.69, after heat treatment at 200 °C. The average pore size is 110 nm. METHODS. Bicontinuous microemulsions with a water:oil ratio of 0.69 were prepared from mixtures of 0.68 g DDAB, 0.72 g tetradecane and 0.50 g of freshly prepared 5 mM Ca^{2+}/25 mM Mg^{2+} supersaturated solution (36:38:26 by weight respectively). A high-water (cubic) phase was prepared by mixing 0.64 g DDAB, 0.12 g tetradecane and 1.2 g of Ca^{2+}/Mg^{2+} solution (34:6:60 by weight, respectively). Electron microscopy was undertaken with a Jeol 1200EX electron microscope. XRD patterns were recorded on a Philips PW-1130 X-ray diffractometer fitted with a Debye–Scherrer camera and Cu Kα radiation.